A global search inversion for earthquake kinematic rupture history: application to the 2000 western Tottori, Japan earthquake

Alessio Piatanesi[1], Antonella Cirella[1], Paul Spudich[2] and Massimo Cocco[1]

[1] Istituto Nazionale di Geofisica e Vulcanologia, Department of Seismology and Tectonophysics, Rome, Italy

[2] US Geological Survey, Menlo Park, CA

Abstract. We present a two-stage nonlinear technique to invert strong motions records and geodetic data to retrieve the rupture history of an earthquake on a finite fault. To account for the actual rupture complexity, the fault parameters are spatially variable peak slip velocity, slip direction, rupture time and rise time. The unknown parameters are given at the nodes of the subfaults, whereas the parameters within a subfault are allowed to vary through a bilinear interpolation of the nodal values. The forward modeling is performed with a discrete wavenumber technique, whose Green's functions include the complete response of the vertically varying Earth structure. During the first stage, an algorithm based on the heat-bath simulated annealing generates an ensemble of models that efficiently sample the good data-fitting regions of parameter space. In the second stage (appraisal), the algorithm performs a statistical analysis of the model ensemble and computes a weighted mean model and its standard deviation. This technique, rather than simply looking at the best model, extracts the most stable features of the earthquake rupture that are consistent with the data and gives an estimate of the variability of each model parameter. We present some synthetic tests to show the effectiveness of the method and its robustness to uncertainty of the adopted crustal model. Finally, we apply this inverse technique to the well recorded 2000 western Tottori, Japan, earthquake (*Mw* 6.6); we confirm that the rupture process is characterized by large slip (3-4 m) at very shallow depths but, differently from previous studies, we imaged a new slip patch (2-2.5 m) located deeper, between 14 and 18 km depth.

1. Introduction

The problem of determining the source parameters of an earthquake has always been a main topic of investigation for earth scientists, extending from hypocenter location to magnitude estimation, moment tensor solution and finite-fault kinematic and dynamic imaging of rupture history. In particular, the pioneering finite-fault inversion methods have been proposed during the early 1980s, mainly to study the 1979 Imperial Valley earthquake (e.g. *Olson and Apsel*, 1982; *Hartzell and Heaton*, 1983 among several others). Since then, progress has been made, especially thanks to the quality and quantity of the available data and the huge growth of the computational capabilities of modern computers. *Liu and Archuleta* (2004) present a useful review of the literature dealing with finite-fault inversion methods.

Thanks to contemporary computational tools, most seismologists are facing the finite-fault inversion in its full non-linear formulation, rather than in a linearized form solved through matrix inversion. Nevertheless, some investigators still prefer to use a linear (or linearized) approach (*Graves and Wald*, 2001; *Semmane et al.*, 2005). In most cases, when non-linear inversion are performed, all parameters are inverted simultaneously using global search method, such as genetic algorithm (e.g. *Emolo and Zollo*, 2005) or simulated annealing (e.g. *Delouis et al.*, 2002; *Ji et al.*, 2002; *Liu and Archuleta*, 2004).

Global search techniques have the ability to escape local minima of the cost function in the parameter space and to converge to the optimal model. The main drawback of the non-linear inversion method is the intrinsic difficulty of assessing error and resolution. Actually, this problem is still unresolved and many authors, from different field of geophysics and seismology, have addressed this difficult matter and have formulated partial or approximated answers (e.g. *Mosegaard and Tarantola*, 1995; *Sambridge*, 1999*; Mosegaard and Sambridge*, 2002; *Kennett*, 2004 and reference therein). From the literature cited above, it seems that in finite-fault

non-linear inversion most computational effort is done to find the optimal model: actually only a few papers deal with some a posterior error analysis. *Emolo and Zollo* (2005) estimated the uncertainty on the source parameters through the analysis of cross-correlation of the misfit function in the neighborhood of the best-fit rupture model. *Peyrat and Olsen* (2004) computed the standard deviation from the 19 models with the smallest misfit; *Liu et al.* (2006) performed 10 inversions that use different seeds for random generation of the starting model and computed the average and standard deviation among the 10 best. We emphasize that estimating the variability of rupture models that are consistent with the data may have important implications, for instance for ground motion prediction through ground shaking scenarios.

In this paper we address the problem of finding the stable characteristics of the earthquake rupture models that are consistent with the data and we give an estimate of the variability of each model parameter. First, we describe our technique to generate an ensemble of models that efficiently sample the good data-fitting regions of parameter space and we show a method to extract the stable features of the rupture model from the previously generated model ensemble. Second, we present two synthetic tests to show the capability of the method to find optimal models. Finally, we apply this two-stage technique to study the 2000 western Tottori earthquake and compare our results with published models.

2. Method

The finite fault is divided into subfaults with model parameters assigned at the corners. However, the value of a parameter is not constant inside a subfault. Rather, it is allowed to vary through a bilinear interpolation of the nodal values, in a way similar to that used by *Liu and Archuleta* (2004) (see also *Beroza and Spudich*, 1988; *Ide and Takeo*, 1997). At each node we give the time of rupture onset, the rise time, the peak slip velocity and the rake angle. Although we are aware that more realistic slip velocity source time functions (STF) can be used (*Tinti et al.*, 2005), in this study we use a simple rectangle function. This slip velocity function has been

used in recent works concerning finite fault inversion problems (e.g. *Emolo and Zollo*, 2005); also, it has been shown that for the 1979 Imperial Valley earthquake, the box-car function gave better waveform fit than an exponential decay function (*Archuleta*, 1984). Our procedure can use different STFs: a parametric investigation on the effect of STFs in finite-fault inversion is discussed in *Cirella et al.*, (2006). In the present implementation of our method, each point on the fault can slip only once, as opposed to multiple time windows approaches in which STFs consist of a sequence of triangles. In these inversions, multiple time windows were used to allow flexibility in the rupture time and rupture velocity (e.g. *Olson and Apsel*, 1982). In our approach variations in rupture velocity are accomplished by making rupture time a variable (see *Cohee and Beroza*, 1994 for a discussion). Also, with a single window we can determine the portion of the data that can be fit with a simple STF as opposed to a complicated and possibly over-parameterized STF.

To obtain ground displacements we use the representation theorem of *Spudich* (1980) to calculate ground motions:

$$\bar{u}_k(\mathbf{x},\omega) = \int_S \bar{\mathbf{s}}(\xi,\omega) \bullet \bar{\mathbf{T}}_k(\xi,\omega;\mathbf{x}) d\xi \qquad (1)$$

where $\mathbf{x}$ is the position of the observer, $\boldsymbol{\xi}$ is the local coordinate system on the fault plane S, k denotes the x, y or z direction, $\bar{u}_k(\mathbf{x},\omega)$ is the Fourier transform of the k-component of displacement at observer location $\mathbf{x}$ and angular frequency ω, $\bar{\mathbf{s}}(\xi,\omega)$ is the Fourier transform of the slip vector at point $\boldsymbol{\xi}$ on the fault and $\bar{\mathbf{T}}_k(\xi,\omega;\mathbf{x})$ is the Fourier transform of the traction vector at a point $\boldsymbol{\xi}$ on the fault caused by a point impulsive force in the k-direction at observer location $\mathbf{x}$. This form of the representation theorem uses Green's function reciprocity.

We calculate the traction Green's functions on the fault plane using a discrete wavenumber integration technique that allows for the complete response in a vertically varying medium (*Olson et al.*, 1984*; Spudich and Xu*, 2003).

The ground displacement (or velocity) at an observer depends non-linearly on the kinematic rupture history. Instead of linearizing the problem and applying linear inverse theory, we use a

global optimization method to search for the source parameters (e.g. *Hartzell and Liu*, 1995; *Ji et al.*, 2002; *Liu and Archuleta*, 2004). In particular we implemented a special flavor of the simulated annealing technique, called the "heat-bath" algorithm (*Rothman*, 1986), which is very efficient for exploring high dimensional model spaces (*Sen and Stoffa*, 1995). The algorithm works by perturbing the model parameters one by one; for this reason, as indicated by *Ji et al.* (2002) and *Liu and Archuleta* (2004), synthetic seismograms from only those subfaults sharing the current nodal parameter need to be updated at each perturbation, thus reducing the computational time.

Since the forward modeling is relatively fast for computing waveform spectra, recorded and synthetic seismograms are compared in the frequency domain, using both real and imaginary parts of the signal's spectra. A main point in inverse problems is the choice of a suitable cost function to represent the goodness of a model. For waveform spectra, we use an objective function that is a hybrid representation between L1 and L2 norm (*Spudich and Miller*, 1990; *Sen and Stoffa*, 1991):

$$E^S(\mathbf{m}) = \frac{1}{N_S}\sum_{i=1}^{N_s} w_i \left[1 - \frac{\sum_{k=1}^{N_f} v_r(\omega_k) v_s^*(\omega_k) + v_r^*(\omega_k) v_s(\omega_k)}{\sum_{k=1}^{N_f} v_r(\omega_k) v_r^*(\omega_k) + \sum_{k=1}^{N_f} v_s(\omega_k) v_s^*(\omega_k)} \right]_i \qquad (2)$$

Here $E^S(\mathbf{m})$ is the cost function corresponding to model $\mathbf{m}$, N_s the number of seismograms, N_f the number of frequencies, v_r and v_s are respectively the recorded and synthetic ground velocity spectra, $*$ symbol stands for complex conjugates, ω_k is the k-th frequency of a ground velocity spectrum and w is a relative weight to be assigned to each record (in this paper we use w=1 and w=0.5 for horizontal and vertical components respectively). This cost function takes information from both the shape and the amplitude of a waveform and it turns out that it is more robust than standard least squares (*Liu and Archuleta*, 2004; *Ji et al.*, 2002).

The cost function E^G, related to near-field GPS measurements, is a sum-squared of the residuals between synthetic and observed static displacements (*Hudnut et al*, 1996), normalized to the observed data:

$$E^G = \frac{1}{N_G} \frac{\sum_{i=1}^{N_G} \left(\frac{d_i^r - d_i^s}{\sigma_i} \right)^2}{\sum_{i=1}^{N_G} (d_i^r)^2} \quad (3)$$

Here N^G is the number of GPS measurements, d^r and d^s are recorded and synthetic displacements respectively and σ is the error associated to the measured data. When we invert simultaneously seismic and GPS observations, the cost function is defined as:

$$E = E^S + E^G \quad (4)$$

Furthermore we do not add special constraints, such as smoothing or moment minimization.

Our algorithm consists of two stages. During the first stage, the heat-bath simulated annealing algorithm explores extensively the model space to generate an ensemble of models that efficiently sample the good data-fitting regions. The simulated annealing technique follows the analogy with annealing in thermodynamics, consisting in slowly cooling the system toward the minimum energy state. Discussing the heat-bath simulated annealing technique is out of the scope of this paper and the interested reader may refer to *Rothman* (1986) and *Sen and Stoffa* (1995) for a detailed presentation. Ideally, large sampling of the model space is achieved by starting the algorithm at relatively high temperature and slowly cooling the system towards the critical temperature, at which the system is expected to reach the minimum energy state (i.e. minimum of the cost function). Since we deal with very large dimension of the model space (typically more than 200 parameters are to be inverted in the following examples) a true simulated annealing cannot be realized, because the ideal cooling would require an excessive CPU time and a simulated quenching is performed instead. In the latter case, the cooling is faster

than in the ideal annealing and the sampling of the model space may be slightly dependent on the choice of the starting model; for this reason the algorithm is conceived to perform several restarts with different random trial models, in order to make the model ensemble independent from a particular choice of the initial model. During the search, all models that are visited and the corresponding values of the cost function $E(\mathbf{m})$ are saved to build the model ensemble Ω. The second stage of our algorithm consists of the ensemble inference. The underlying idea is that basing inferences on an ensemble of potential solutions conveys more information than considering just the best. In fact, limiting the analysis to the features present in only the best fitting model is often insufficient because of nonuniqueness in the problem and noise in the data (e.g. *Sen and Stoffa*, 1995; *Sambridge*, 2001; *Kennett*, 2004 and references therein).

Following the work of *Shibutani et al.* (1996), we compute an averaged model parameter and the associated standard deviation by weighting all models of the ensemble by the inverse of their cost function values. Let m_{ij} be the i-th parameter of the j-th model belonging to the ensemble Ω and E_j the cost function corresponding to the model $\mathbf{m}_j$. The averaged model parameter $\langle m_i \rangle$ and the corresponding standard deviation $\langle \sigma_i \rangle$ can be written as:

$$\langle m_i \rangle = \frac{\sum_{j \in \Omega} m_{ij} / E_j}{\sum_{j \in \Omega} 1 / E_j} \tag{5}$$

$$\langle \sigma_i \rangle^2 = \frac{\sum_{j \in \Omega} \left[m_{ij} - \langle m_i \rangle \right]^2 / E_j}{\sum_{j \in \Omega} 1 / E_j} \tag{6}$$

The estimates $<m_i>$ and $<\sigma_i>$ represent the ensemble properties and are the actual solution of our nonlinear inverse problem. This model assessment is different from those proposed in previous work. *Peyrat and Olsen* (2004) computed the standard deviation from the 19 models with the smallest misfit; *Liu et al.* (2006) performed 10 inversions that use different seeds for random generation of the starting model and computed the average and standard deviation among the 10 best models. The novelty of our approach is the use of a very large model ensemble, built up by means of multiple restarts of the annealing algorithm, to take advantage from the whole search process instead of looking only at the best models.

3. Synthetic tests

In order to discuss the applicability and the main features of the proposed method, we present in this section the results of two synthetic tests. We take the fault geometry and station distribution of the Tottori earthquake (see Fig.1) and we construct a fairly complicated target rupture model to generate the synthetic dataset. The fault has the following geometrical parameters: strike is 150°, dip is 90°, length and width are 40 km and 20 km, respectively; the top of the fault is 0.5 km below the free surface. Slip is concentrated only on two main asperities, A and B (see Fig.2). Asperity A has a peak slip velocity of 1.45 m/s, rake angle of 45° and a rise time of 3.0 s; asperity B is narrower and extends deeper than A, has 1.5 m/s of peak slip velocity, rake angle of 0° and a rise time of 3.0 s. The rupture front propagates at 2.5 km/s, except in the upper left part of the fault, where it is propagating at nearly 3.5 km/s. We invert simultaneously all parameters at nodal points equally spaced along strike and dip every 4 km (see Fig. 2). During the inversion, bounds of 0 to 2.5 m/s with 0.25 m/s interval are allowed for the peak slip velocity; the rise time varies from 1 to 4 sec at 0.5 sec interval; the rake angle goes from -45° to 45° by steps of 5°; the rupture time of each grid node is bounded by the times for a rupture to reach the node traveling at 2 and 4 km/s from the hypocenter.

3.1 Noise-free data

Adopting the crustal model listed in Table1, we compute synthetic ground velocities in the frequency band 0.05-0.7 Hz (see Fig.4a), which is the same band we will use later in the application to the real data of the Tottori earthquake, and we compute horizontal components of static displacement (see Fig.5a) and use these as our dataset. During the first stage of the inversion, we generate a model ensemble by exploring about one million rupture models; then, through eq.(5), we compute the averaged rupture model (Fig.3a). The inverted model is very similar to the target one; the positions of the two asperities are correctly imaged and the peak slip velocity well estimated. The rise time is also precisely retrieved and the faster propagation of the rupture front, on the upper left side, is caught fairly well. Finally, the rake angle of asperity A is very well constrained, whereas we notice some discrepancies in asperity B. Although similar, the target and inverted models are not identical. Nevertheless the cost function of the inverted model is very low (E=0.007 and E=0.009 for the best and the average model respectively) and the comparison of the waveforms and horizontal displacements reveals (as expected) an almost perfect match between data and synthetics (Fig. 4a and Fig. 5a). Considering that the data are noise free, this indicates that the inverse problem is intrinsically non unique. By means of eq.(6) we also calculate the standard deviation $<\sigma_i>$ for each parameter of the averaged rupture model. We take advantage of the perfect knowledge of the target model to assess to what extent the computed standard deviations are good estimates of the true errors; in Fig. 6a we show the value of the parameters of the target and inverted model as well as its standard deviation, taken at some control points (black dots in Fig. 2). We may see that the target model lies within one standard deviation, thus indicating that the standard deviations are slightly large proxies for the true errors. In (Fig.7a) we show the standard deviations on the whole fault plane: in general, the smaller the value of $<\sigma_i>$, relatively to $<m_i>$, the smaller the error. For this synthetic test, the standard deviations corresponding to the two asperities are very small, thus indicating small error in the model. It should be noted that large standard deviations correlate to zones of the fault with

low or no slip; this is not surprising, since those parts of the fault do not contribute to the ground motion and cannot be constrained by the data inversion.

3.2 Uncertainty of the velocity structure

Several authors pointed out that inaccurate knowledge of the velocity structure represents a main source of error in finite-fault inversion (*Graves and Wald*, 2001; *Wald and Graves*, 2001; *Ji et al.*, 2002; *Liu and Archuleta*, 2004). In fact the crustal model directly affects the calculation of the Green's functions that are used to compute the ground motion. Here we study the robustness of our method to a reasonable uncertainty in the velocity structure. To this goal we consider two different velocity structures that are listed in Table 1 (DPRI model) and Table 2 (PK model). The first is the crustal model used for the hypocenter determination by the Research Center for Earthquake Prediction – Disaster Prevention Research Institute, Kyoto. The second is a modified version, proposed by *Pulido and Kubo* (2004) on the basis of P and S waves velocities measured at shallow depth at several boreholes sites of Kik-Net strong motion network. The two velocity structures differ in the number of layers and in the velocities of both P and S waves, the PK model being about 10% slower than DPRI model. We use the PK model and the target rupture model described in the previous section to compute the synthetic seismograms in the frequency band 0.05-0.7 Hz and the horizontal component of static displacements representing our virtual dataset. The DPRI model is then used to calculate the Green's functions to be used in the inversion. Throughout the search stage, the inversion algorithm explores about 3 millions rupture models to build up the model ensemble; then, as in the previous test, we make statistical inferences on this ensemble by computing the average rupture model $<m_i>$ and the corresponding standard deviation $<\sigma_i>$. The cost function for the best and the average model is E=0.1 and E=0.14 respectively. The inverted model (Fig.3b) still shows two distinct patches, with peak slip velocity and rise time respectively of the order of 1.5 m/s and 2.5 s. The rake angle seems to be robustly inverted, especially over asperity A and the rupture times still show a faster propagation

in the upper left side of the fault, though it is less evident than in the previous test. However, both asperities are smeared, and in particular the slip is significantly increased at very shallow depth. This confirms some of the results proposed by *Ji et al.* (2002), who find that the near-surface slip estimate is strongly affected by the velocity structure. Furthermore we note that the two slip patches are somewhat mislocated; this feature is more evident for asperity B, which is shifted to the right by about 2 km. The uncertainty in the velocity structure increases the nonuniqueness of the inverse problem, i.e. instead of only one solution we have many rupture models that are consistent with the data. This reflects on the averaged rupture model of Fig.3b: for instance, differently from what we found in the previous noise-free test, now the model solution shows a low to intermediate amount of slip distributed between the two patches. This means that many models, with a diffused slip on the fault plane, are still consistent with the data (Fig.4b and Fig.5b). Errors in the velocity structure also increase the standard deviation of the averaged model (Fig. 6b); in this case the target model lies between one standard deviation only in those regions characterized by large slip. From Fig. 7b we may also see a global decrease of the resolution with respect to the noise-free case study. It seems that the computed standard deviations are good estimates of actual error when the Green's functions are sufficiently accurate, and that the computed standard deviations will underestimate the true error when inaccurate Green's functions are used. The standard deviations may be seen as bounds that delineate a consistency region of the rupture model.

4. The application to the 2000 western Tottori (Japan) earthquake

The Tottori, Japan, earthquake (M_W=6.6) occurred on October 6, 2000 at 04:30:17.75 UTC. The epicenter is located at 35.275°N and 133.350°E (*Fukuyama et al.*, 2003). This earthquake is a predominantly strike slip event for which a large number of both surface and borehole strong motion records as well as several GPS measurements of the surface displacement (*Sagiya et al.*, 2002) are available. We select 18 accelerometric stations that do not seem to be strongly

contaminated by site effects and that offer a good azimuthal coverage and 13 GPS stations (shown in Fig.1). We band-pass filter the recorded ground velocities between 0.05 and 0.7 Hz with a two pole and two pass Butterworth filter and we carefully verify that no spurious effect of the filter is introduced in the waveforms. The lower bound of the frequency band is determined by instrument capability; we observe that below 0.05 Hz several waveforms reveal some instabilities, such as small linear trends that arise during the strongest motion. The upper frequency limit is controlled by crustal model and fault discretization; with our model parametrization, the frequency content of the synthetic waveforms is negligible above 0.7 Hz. The fault is 40 km long and 20 km wide, with a dip of 90° and the top border at 0.5 km depth. The hypocentral depth is 12.5 km, a value that is between 9.5 km as determined by *Fukuyama et al.* (2003) and 14.5 km as reported in *Semmane et al.* (2005). We invert simultaneously all parameters at nodal points equally spaced along strike and dip every 4 km.

During the inversion, bounds of 0 to 2.5 m/s with 0.25 m/s interval are allowed for the peak slip velocity; the rise time varies from 1 to 5 sec at 0.5 sec interval; the rake angle goes from -15° to 15° by steps of 5°; the rupture time of each grid node is bounded by the times for a rupture to reach the node traveling at 2 and 4 km/s from the hypocenter.

Since we have no strong reasons to favor the DPRI or PK velocity structure (see Table 1 and Table 2), we perform a separate search stage for each structure and we generate two model ensembles. Then we merge these ensembles to build up a larger one (about 7 million of models) on which we make statistical inferences. In this way we incorporate some degree of uncertainty of the crustal structure in the inversion procedure.

The weighted average model (Fig.8) shows a patch of high slip velocity of the order of 1.5-1.75 m/s that extends from the upper border down to a depth of 6 km with a length of about 12-14 km; this patch is somewhat slightly diffused to the south-east along the down-dip direction. A smaller region of relatively high slip velocity of about 0.75-1.0 m/s is located deeper, between 14 and 18 km depth, about 12 km north-west from the hypocenter. Over the hypocenter and its

surrounding region, the fault does not seem to have slipped significantly. The seismic moment of the average model is M_0=1.7*10^{19} Nm, that is comparable with M_0=1.6-1.7*10^{19} found by *Semmane et al.* (2005). The rake angle indicates a basically pure left-lateral strike slip mechanism, with very small fluctuating dip component. The rupture velocity does not change strongly on the fault plane; we find that the propagation is slightly faster along the strike (v_r=2.6 km/s, corresponding to 70% of the shear wave velocity) than along the up-dip direction (v_r=2.2 km/s, corresponding to 63% of the mean shear wave velocity). Note that the lack of variation in the rupture front contours reflects the fact that the final model is an average model over many individual models in which the rupture front may be more irregular. The total duration of the rupture is about 8 s. Furthermore, the rupture propagation appears remarkably indifferent to the slip release. Overall, the rupture model appears quite smooth, mainly due to the averaging process on the model ensemble; on the contrary the best model is rougher than the averaged one. The comparison of the recorded and synthetic waveforms (Fig.9a) shows a satisfactory agreement, though in some stations the high frequencies are not well reproduced (Fig. 9b): this is probably due to site effects that are not modeled in our calculations. Furthermore, the synthetic horizontal displacements match well with GPS vectors both in amplitude and direction (Fig. 10).

4.1 Discussion

As we did in the previous sections dealing with the synthetic tests, we also compute the standard deviations of the model parameters $<\sigma_i>$, that we show in Fig.11. If we focus our attention on the regions of the fault that are characterized by large slip values, we may appreciate that the rupture model is stably inverted there. In fact, the standard deviations $<\sigma_i>$ are 3 to 5 times smaller than the corresponding averages of model parameters $<m_i>$; this indicates that the inverted model represents the major features of the rupture process quite well. On the other hand, if we look at those regions of the fault that are characterized by low and diffused slip, we may have an estimate of the sensitivity threshold of the data; a slip velocity of about 0.3-0.4 m/s (the

minimum standard deviation of the slip velocity) is allowed anywhere on the fault, defining a class of rupture models still consistent with the data.

The most striking feature of the inverted rupture model is the large coseismic slip at very shallow depth, in agreement with the results obtained by other investigators *(Iwata and Sekiguchi,* 2002; *Semmane et al*., 2005; *Festa and Zollo*, 2006). Also the slip distribution from the main shallow patch to the south-east and down-dip direction has been observed by the above investigators. However, differently from other studies, we found significant slip north-west of the hypocenter, between 14 and 18 km depth. This part of the fault is characterized by peak slip velocity and rise time of about 1.0 m/s and 2.5 s respectively, thus yielding a mean slip of 2.5 m. Though this patch contributes less than the shallow one to the ground motion, nevertheless it is a robust feature of the rupture process. Considering the standard deviations of peak slip velocity and rise time corresponding to this patch, respectively of 0.5 m/s and 0.7 s, we may calculate lower (0.9 m) and upper (4.8 m) bounds for the slip amplitude. Intrigued by this characteristic of our rupture model, we analyzed in some detail the search process that builds-up the model ensemble. We found that the shallow patch of large slip and its elongation to the south-east and down-dip direction are the features of the rupture model that are grasped first during the search stage; these models are probably located in a wide and local minimum of the cost function ($E \sim 0.5$). Beyond this, as the algorithm goes on in the search of the model space, it encounters a new cluster of models featuring a second slip concentration at depth and characterized by lower value of the cost function (E_{best} =0.31; E_{average} = 0.35). These last models are probably located in a narrow and deep minimum of the cost function, hardly accessible by linear and/or linearized inverse method.

5. Conclusion

We have presented a method to solve the finite-fault non-linear inverse problem, which consists of retrieval of the complete rupture history on a finite fault using seismic and geodetic data. This problem, owing to azimuthal gaps in the station distribution, limited frequency bandwidth,

uncertainty of the crustal structure, site effects and fault parameterization, is known to have non-unique solutions. Actually, the main source of uncertainty in finite-fault inversion is the choice of the Earth model to compute the Green's functions. In their conclusion, *Liu and Archuleta* (2004) state that "a prudent approach is to use each Earth model that is available to deduce the range of possible faulting models and look for the elements that are common to the different Earth models". Our procedure directly implements such a strategy, since the a posteriori ensemble inference is conceived to extract the most stable features of the earthquake rupture that are consistent with the data, rather than simply searching for the best model. We have applied this inverse technique to the 2000 Tottori, Japan earthquake, using waveforms in the frequency band 0.05-0.7 Hz recorded by 18 accelerometers and using horizontal static displacements measured at 13 GPS sites. We have confirmed that the rupture process is characterized by large slip (3-4 m) at very shallow depths, from the top of the fault down to a depth of 6 km. However, thanks to the ability of this inverse technique to escape local minima of the cost function, we imaged a slip patch (2-2.5 m) located deeper, between 14 and 18 km depth, not inferred by previous studies. The relatively small standard deviations of the corresponding parameters, computed through the ensemble inference, indicate that this slip patch is a real feature of the rupture history.

Another advantage of the ensemble inference is the possibility of estimating the variability of rupture models that are consistent with the data. In particular we may evaluate lower and upper bounds for some source parameters, such as peak slip velocity and rupture speed. This may have important implications, for instance for ground motion prediction through ground shaking scenarios.

We believe that the appraisal stage in non-linear inversion is as important as the search for the best model. This appraisal should be further developed and become a common practice in finite-fault nonlinear inversion studies.

Acknowledgments. The authors are grateful to Rodolfo Console, Antonio Emolo and an anonymous reviewer for their suggestions that greatly improved the paper. Thanks to K-net and KiK-net for providing strong motion data and to Takeshi Sagiya for providing GPS data. Thanks to Fabrice Cotton and Eiichi Fukuyama for their help with GPS data. Some figures are made using Generic Mapping Tools free software (*Wessel and Smith*, 1998).

References

Archuleta, R. J. (1984), A faulting model for the 1979 Imperial Valley earthquake, *J. Geophys. Res.*, 89, 4559-4585.

Beroza, G.C. and P. Spudich (1988), Linearized inversion for fault rupture behaviour: application to the 1984 Morgan Hill, California, earthquake, *J. Geophys. Res.,* 93(B6), 6275-6296.

Cirella, A., A. Piatanesi, E. Tinti and M. Cocco (2006), Dynamically consistent source time functions to invert kinematic rupture histories, *Eos, Trans. AGU 87*(52), Fall Meet. Suppl., Abstract S41B-1323.

Cohee, B.P. and G.C. Beroza (1994), A comparison of two methods for earthquake source inversion using strong motion seismograms, *Annali di Geofisica,* 37, 6, 1515-1538.

Delouis, B, Giardini D., Lundgren P. and Salichon J. (2002), Joint inversion of Insar, GPS, teleseismic and strong-motion data for the spatial and temporal distribution of earthquake slip: application to the 1999 Izmit mainshock, *Bull. Seismol. Soc. Am.,*92(1), 278-299.

Emolo, A. and A. Zollo (2005), Kinematic source parameters for the 1989 Loma Prieta earthquake from the nonlinear inversion of accellerograms, *Bull. Seismol. Soc. Am.*, 95(3), 981-994, doi:10.1785/0120030193.

Festa, G. and Zollo A. (2006), Fault slip and rupture velocity inversion by isochrone backprojection, *Geophys. J. Int.*, 166, 745-756, doi:10.1111/j.1365-246X.2006.03045.x

Fukuyama, E., W.L. Ellsworth, F. Waldhauser and A. Kubo (2003), Detailed fault structure of the 200 western Tottori, Japan, earthquake sequence, *Bull. Seismol. Soc. Am.*, 93, 14-68-1478.

Graves, R.W. and D.J Wald (2001), Resolution analysis of finite source inversion using one- and three-dimensional Green's functions: 1. Strong motions, *J. Geophys. Res.*, 106(B5), 8745-8766.

Hartzell, S. and T. H. Heaton (1983), Inversion of strong ground motion and teleseismic waveform data for the fault rupture history of the 1979 Imperial Valley, California earthquake, *Bull.Seismol. Soc. Am.*, 73, 1553-1583.

Hartzell, S, and P. Liu, (1995), Determination of Earthquake Source Paramenters Using a Hybrid Global Search Algorithm *Bull. Seismol. Soc. Am.*, 85, 516 - 524

Hudnut, K.W., Y. Bock, M. Cline, P. Fang, J. Freymuller, K. Gross, D. Jackson, S. Larson, M. Lisowski, Z. Shen and J. Svarc (1996): Coeismic displacements of the 1994 Northridge, California earthquake, *Geol. Soc. Am. Bull.*, 86, no. 1B, S19-S36.

Ide, S. and M. Takeo (1997): Determination of constitutive relations of fault slip based on seismic wave analysis, *J. geophys. Res.*, 102(B12), 27379-27391.

Iwata, T and H. Sekiguchi (2002), Source process and near-source ground motion during the 2002 Tottori-ken-Seibu earthquake , *Proc. 11th Japan Erthq. Eng. Symp.*, 125-128, (in japanease with english abstract).

Ji, C., D. J. Wald, and D. V. Helmberger (2002), Source description of the 1999 Hector Mine, California, earthquake, Part I: Wavelet domain inversion theory and resolution analysis, *Bull. Seismol. Soc. Am.*, 92 (4), 1192-1207.

Kennet, B.L.N. (2004), Consistency regione in non-linear inversion, *Geophys. J. Int.*, 157, 583-588.

Liu, P., and R. Archuleta (2004), A new nonlinear finite fault inversion with three-dimensional Green's functions: application to the 1989 Loma Prieta, California, earthquake, *J.Geophys. Res.*, 109, B02318, doi:10.1029/2003JB002625.

Liu, P., S. Custodio and R. J. Archuleta (2006), Kinematic inversion of the 2004 M 6.0 Parkfield earthquake including an approximation to site effects, *Bull. Seismol. Soc. Am.*, 96, 4B, S143-S158, doi:10.1785/0120050826.

Mosegaard, K. And M. Sambridge (2002), Monte Carlo methods in geophysical inverse problem, *Rev. Geophys.*, 40(3), 1-29.

Mosegaard, K. And A. Tarantola (1995), Monte Carlo sampling of solutions to inverse problema, *J. Geophys. Res.*, 100(B7), 12431-12447.

Olson A.H. and R.J. Apsel (1982), Finite fault and inversion theory with application to 1979 Imperial Valley earthquake, *Bull. Seismol. Soc. Am.*, 72, 1969-2001.

Olson, A.H., J.A. Orcutt, and G.A. Frasier (1984), The discrete wavenumber / finite element method for synthetic seismograms, *Geophys. J. R. Astr. Soc.*, 77, 421-460.

Peyrat, S. and K.B. Olsen (2004), Nonlinear dynamic rupture inversion of the 2000 Western Tottori, Japan, earthquake, *Geophys. Res. Lett.*, 31, L05604, doi:10.1029/2003GL019058.

Pulido, N. and T. Kubo (2004), Near-fault strong motion complexity of the 2000 Tottori earthquake (Japan) from a broadband source asperity model, *Tectonophysics*, 390, 177-192.

Rothman, D. (1986), Automatic estimation of large residual statics corrections, *Geophysiscs*, 51, 332-346.

Sagiya, T., T. Nishimura, Y. Hatanaka, E. Fukuyama and W.L. Ellsworth (2002), Crustal movements associated with the 200 western Tottori earthquake and its fault models, *ZiSin (J. Seismol. Soc. Jpn.)* 54, 523-534 (in Japanese with English abstract).

Sambridge, M. (1999), Geophysical inversion with a neighbourhood algorithm-II. Appraising the ensemble, *Geophys. J. Int.* 138, 727-746.

Sambridge, M. (2001), Finding acceptable models in nonlinear inverse problems using a neighbourhood algorithm, *Inverse Problems*, 17, 387-403.

Semmane, F., F. Cotton and M. Campillo (2005), The 2000 Tottori earthquake: a shallow earthquake with no surface rupture and slip properties controlled by depth, *J. Geophys. Res.*, 110, B03306, doi:10.1029/2004JB003194.

Sen, M. and Stoffa P.L. (1991), Nonlinear one-dimensional seismic waveform inversion using simulated annealing, *Geophysics*, 56,1624-1638.

Sen, M. and Stoffa P.L. (1995), *Global Optimization Methods in Geophysical Inversion*, Adv. Explor. Geophys., vol. 4, Elsevier Sci., New York.

Shibutani, T., M. Sambridge and B. Kennett (1996), Genetic algorithm inversion for receiver functions with application to crust and uppermost mantle structure beneath Eastern Australia, *Geophys. Res. Lett.*, 23(14), 1829-1832.

Spudich, P. (1980), The DeHoop-Knopoff representation theorem as a linear inversion problem, *Geophys. Res. Lett.*, 9, 717-720.

Spudich, P., and D.P. Miller (1990), Seismic site effects and the spatial interpolation of earthquake seismograms: Results using aftershocks of the 1986 North Palm Springs, California, earthquake, *Bull. Seismol. Soc. Am.*, 80(6), 1504-1532.

Spudich, P. and L. Xu (2003), Software for calculating earthquake ground motions from finite faults in vertically varying media, in *International Handbook of Earthquake and Engineering Seismology*, Academic Press.

Tinti, E., E. Fukuyama, A. Piatanesi and M. Cocco (2005), A kinematic source time function compatible with earthquake dynamics, *Bull. Seismol. Soc. Am.*, 95(4), 1211-1223, doi:10.1785/0120040177.

Wald, D.J. and R.W. Graves (2001), Resolution analysis of finite source inversion using one- and three-dimensional Green's functions: 2. Combining seismic and geodetic data, *J. Geophys. Res.*, 106(B5), 8767-8788.

Wessel, P. and W.H.F. Smith (1998), New, improved version of the Generic Mapping Tools released, *EOS Trans. AGU*, 79, 579.

A. Piatanesi, A. Cirella and M. Cocco, Istituto Nazionale di Geofisica e Vulcanologia, Via di Vigna Murata 605, 00143 Rome, Italy. (e-mail: piatanesi@ingv.it, cirella@ingv.it, cocco@ingv.it)

P. Spudich, U.S. Geological Survey, 345 Middlefield Road, Menlo Park, CA, 94025 USA. (email: spudich@usgs.gov)

(Received …; revised …; accepted ….)

Table 1. Velocity Structure of the Tottori region (DPRI model)*

depth (km)	Vp (km/s)	Vs (km/s)	d (kg/m^3)
0	5.50	3.179	2600
2	6.05	3.497	2700
16	6.60	3.815	2800
38	8.03	4.624	3100

Table 2. Velocity Structure of the Tottori region (PK model, *Pulido and Kubo,* 2004)*

H (km)	Vp (km/s)	Vs (km/s)	d (kg/m^3)
0	5.20	3.002	2600
3	5.70	3.290	2700
7	6.00	3.464	2750
16	6.60	3.815	2800
38	6.80	3.926	3100

* Material properties interpolated linearly between given depths

Figure captions

Figure 1. Map of the fault geometry of the 2000 Western Tottori, Japan earthquake. The black solid line represents the fault trace of the plane adopted in this study. Black star indicates the epicenter. White triangles and inverted triangles represent K-Net (surface sensor) and Kik-Net (borehole sensor) strong motion stations respectively. Black dots represent GPS stations.

Figure 2. Target rupture model used for synthetic tests. Horizontal axis is along-strike distance measured from the epicenter. Vertical axis is down-dip distance measured from the ground surface. Top panel shows the grid nodes (open circles) together with the control points used to draw Fig. 5 (solid circles with numbers). Middle panel shows the rise time as gray shadows; rupture time shown by contour lines (in seconds). Bottom panel shows peak slip velocity as gray shadows; rupture time shown by contour lines (in seconds). Arrows represent the slip vector. The slip patches are denoted by capital letters A and B (see text for details).

Figure 3. Inverted rupture model (average model from ensemble inference) from the synthetic tests. a) inversion with noise-free data; b) inversion with crustal structure uncertainty. Top panels show the rise time as gray shadows; rupture time shown by contour lines (in seconds). Bottom panels show peak slip velocity as gray shadows; rupture time shown by contour lines (in seconds). Arrows represent the slip vector .

Figure 4. Comparison of synthetic ground velocities from the target rupture model (solid lines) with the inverted rupture model (dotted lines). Numbers with each trace are peak velocity of the synthetic line (in cm/s). Waveforms are computed in the frequency band 0.05-0.7 Hz. a) inversion of noise-free data; b) inversion with crustal structure uncertainty.

Figure 5. Comparison of synthetic horizontal displacements from the target rupture model (black arrows) with the inverted rupture model (white arrows). a) inversion of noise-free data; b) inversion with crustal structure uncertainty.

Figure 6. Comparison of peak slip velocity (upper panels) and rise time (lower panels) for the target and inverted rupture model. Numbers along the abscissa indicate the control points shown in Fig. 2. Vertical bars represent ± one standard deviation. a) inversion with noise-free data; b) inversion with crustal structure uncertainty.

Figure 7. Standard deviation of average model, computed through ensemble inference; contour lines represent total slip displacement in meters, but in third row panels where rupture times (in seconds) are plotted instead; a) inversion with noise-free data; b) inversion with crustal structure uncertainty.

Figure 8. Inverted rupture model (average model from ensemble inference) of the 2000 western Tottori earthquake. Top panel shows the rise time. Middle panel shows the peak slip velocity; rupture time shown by contour lines (in seconds); arrows represent the slip vector. Bottom panel shows the total slip displacement.

Figure 9. Comparison of recorded strong motions (solid lines) with synthetic waveforms computed from the inverted rupture model of Fig.7 (dotted lines). Both records and synthetics are filtered in the frequency band 0.05-0.7 Hz. a) comparison in the time domain; b) comparison in the frequency domain. Numbers with each trace are peak amplitude of the synthetic line in cm/s and in cm for the waveforms and the spectra respectively.

Figure 10. Comparison of measured (black arrows) with synthetic (white arrows) horizontal displacements.

Figure 11. Standard deviation of the average rupture model of the Tottori earthquake (shown in Fig.8), computed through ensemble inference. Contour lines represent total slip displacement in meters, but in third row panels where rupture times (in seconds) are plotted instead;

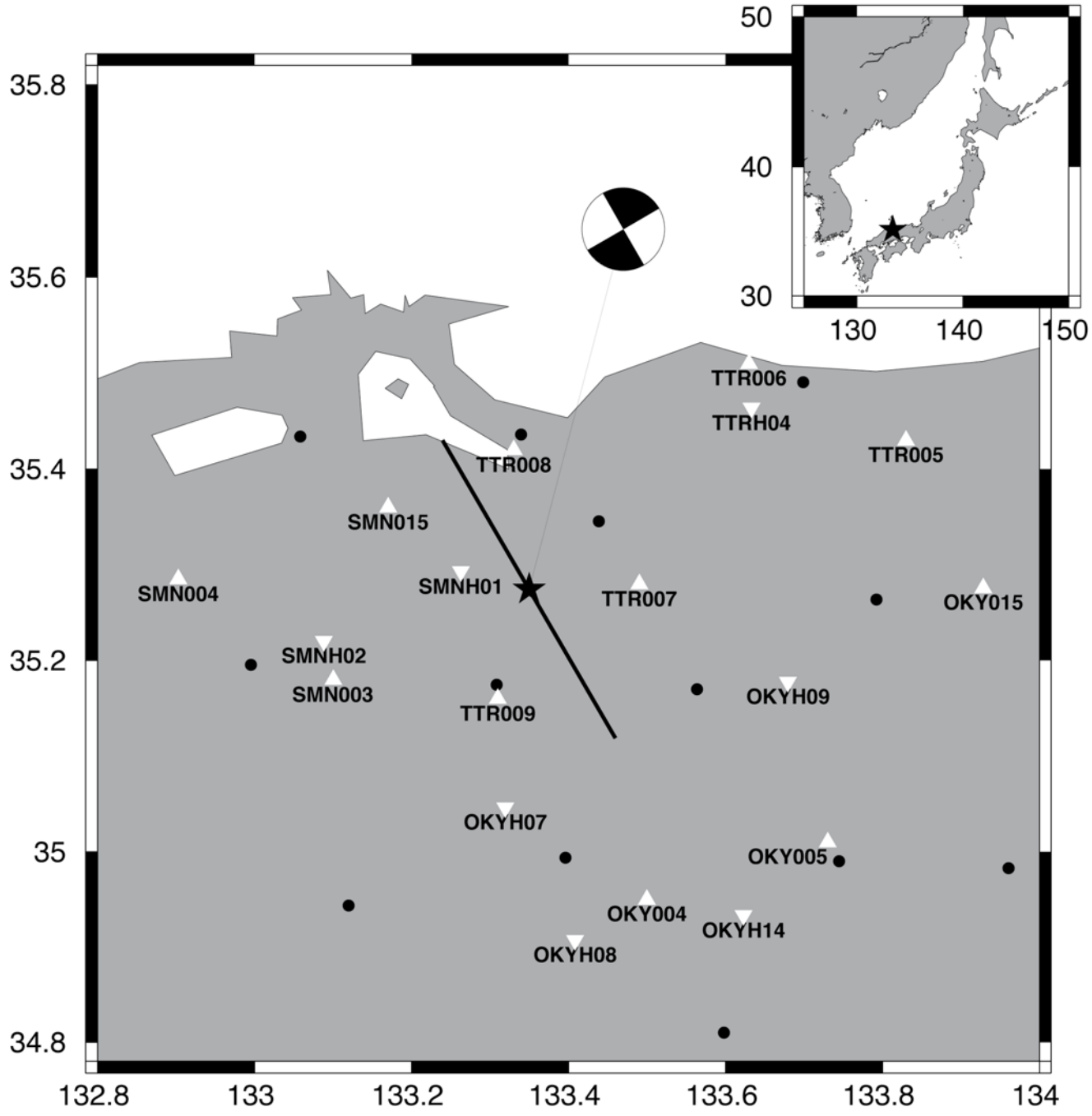
50
40
30
130
140
150
35.8
35.6
35.4
35.2
35
34.8
132.8
133
133.2
133.4
133.6
133.8
134
TTR006
TTRH04
TTR005
TTR008
SMN015
SMN004
SMNH01
TTR007
OKY015
SMNH02
SMN003
TTR009
OKYH09
OKYH07
OKY005
OKY004
OKYH14
OKYH08

Figure 1

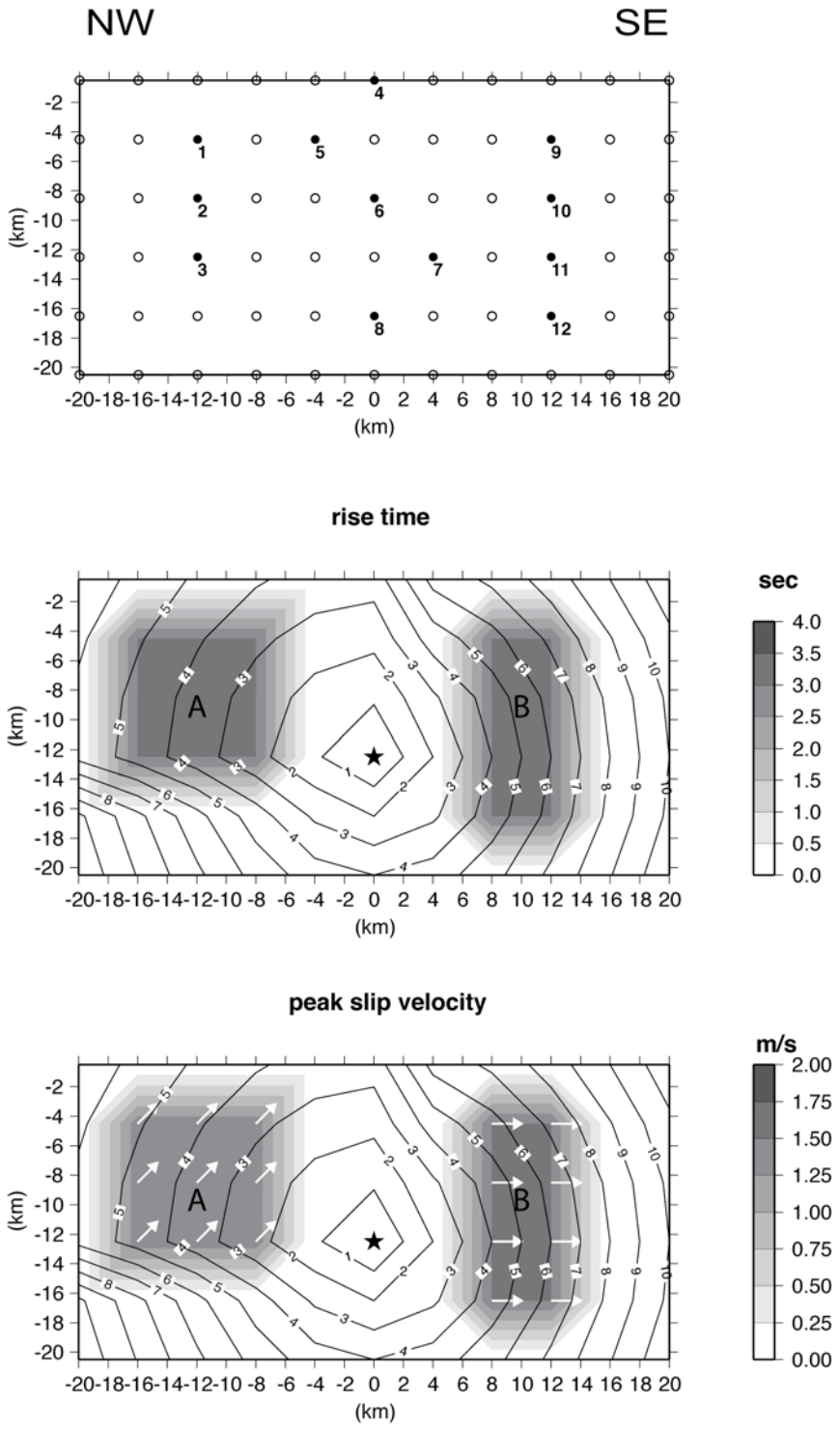
NW
SE
(km)
(km)
rise time
sec
4.0
3.5
3.0
2.5
2.0
1.5
1.0
0.5
0.0
A
B
peak slip velocity
m/s
2.00
1.75
1.50
1.25
1.00
0.75
0.50
0.25
0.00

Figure 2

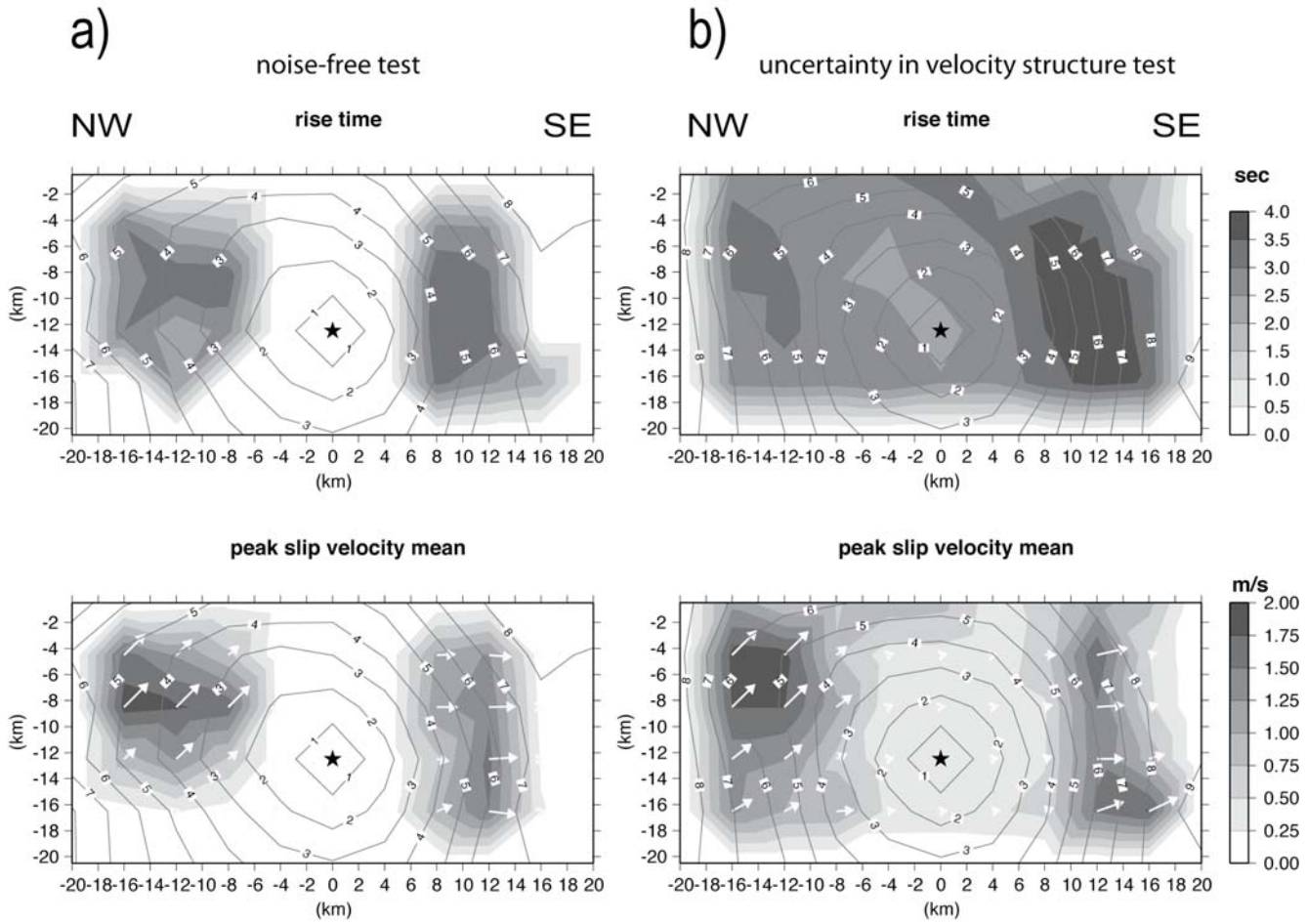
a)
noise-free test
b)
uncertainty in velocity structure test
NW
rise time
SE
NW
rise time
SE
sec
4.0
3.5
3.0
2.5
2.0
1.5
1.0
0.5
0.0
(km)
(km)
peak slip velocity mean
peak slip velocity mean
m/s
2.00
1.75
1.50
1.25
1.00
0.75
0.50
0.25
0.00
(km)
(km)

Figure 3

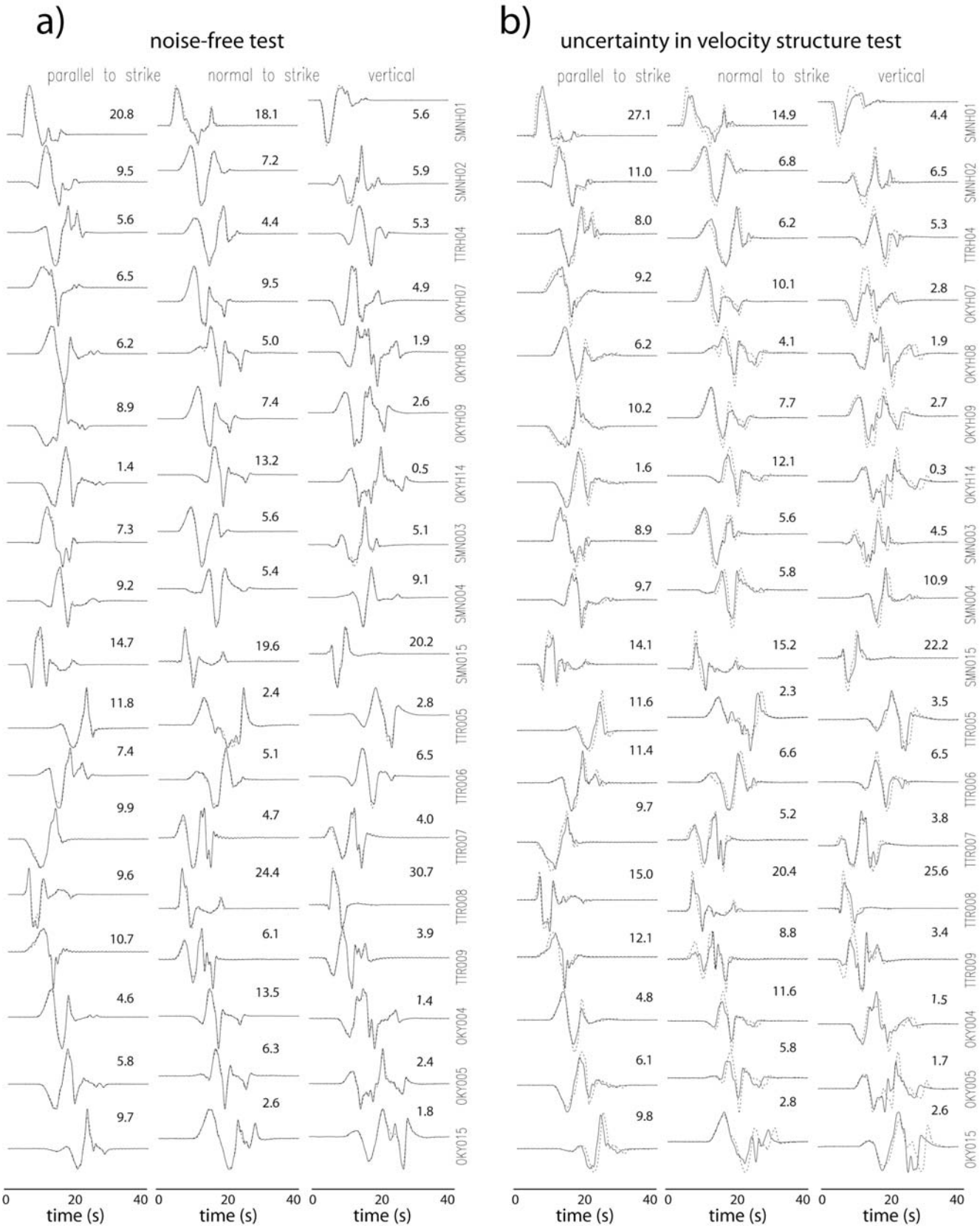
a)
noise-free test
parallel to strike
normal to strike
vertical
20.8
18.1
5.6
9.5
7.2
5.9
5.6
4.4
5.3
6.5
9.5
4.9
6.2
5.0
1.9
8.9
7.4
2.6
1.4
13.2
0.5
7.3
5.6
5.1
9.2
5.4
9.1
14.7
19.6
20.2
11.8
2.4
2.8
7.4
5.1
6.5
9.9
4.7
4.0
9.6
24.4
30.7
10.7
6.1
3.9
4.6
13.5
1.4
5.8
6.3
2.4
9.7
2.6
1.8
SMNH01
SMNH02
TTRH04
OKYH07
OKYH08
OKYH09
OKYH14
SMN003
SMN004
SMN015
TTR005
TTR006
TTR007
TTR008
TTR009
OKY004
OKY005
OKY015
0
20
40
time (s)
b)
uncertainty in velocity structure test
parallel to strike
normal to strike
vertical
27.1
14.9
4.4
11.0
6.8
6.5
8.0
6.2
5.3
9.2
10.1
2.8
6.2
4.1
1.9
10.2
7.7
2.7
1.6
12.1
0.3
8.9
5.6
4.5
9.7
5.8
10.9
14.1
15.2
22.2
11.6
2.3
3.5
11.4
6.6
6.5
9.7
5.2
3.8
15.0
20.4
25.6
12.1
8.8
3.4
4.8
11.6
1.5
6.1
5.8
1.7
9.8
2.8
2.6
SMNH01
SMNH02
TTRH04
OKYH07
OKYH08
OKYH09
OKYH14
SMN003
SMN004
SMN015
TTR005
TTR006
TTR007
TTR008
TTR009
OKY004
OKY005
OKY015
0
20
40
time (s)

Figure 4

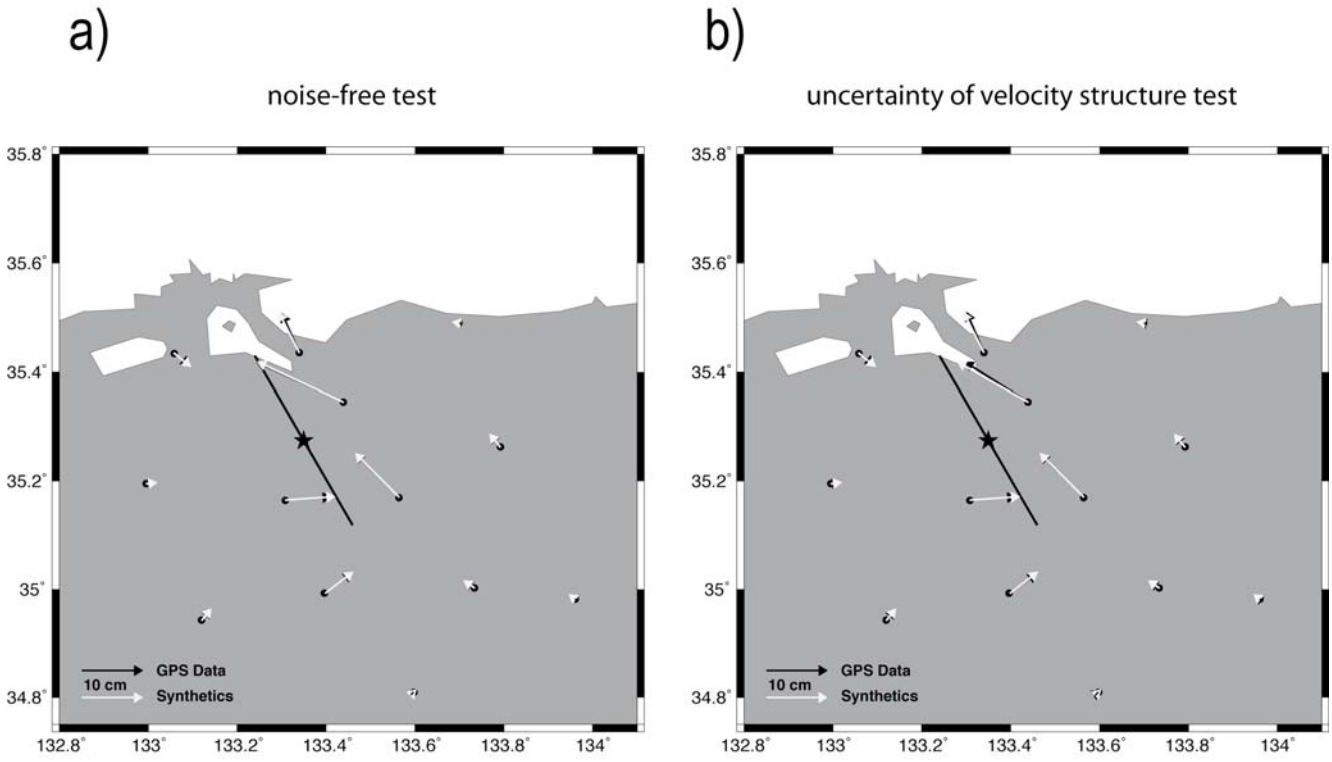
a)
noise-free test
b)
uncertainty of velocity structure test
35.8°
35.6°
35.4°
35.2°
35°
34.8°
132.8°
133°
133.2°
133.4°
133.6°
133.8°
134°
GPS Data
10 cm
Synthetics

Figure 5

1

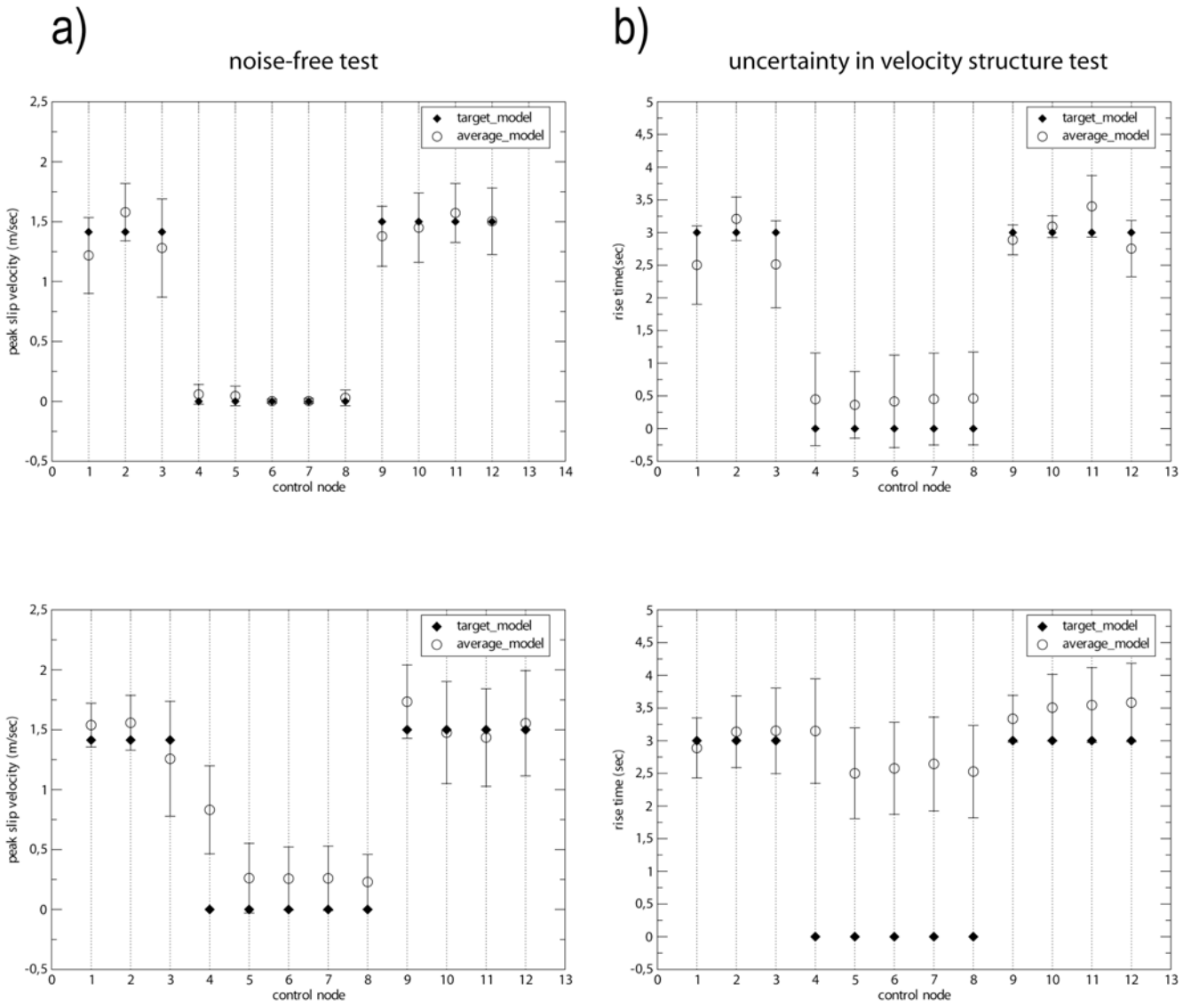

2

3 Figure 6

4

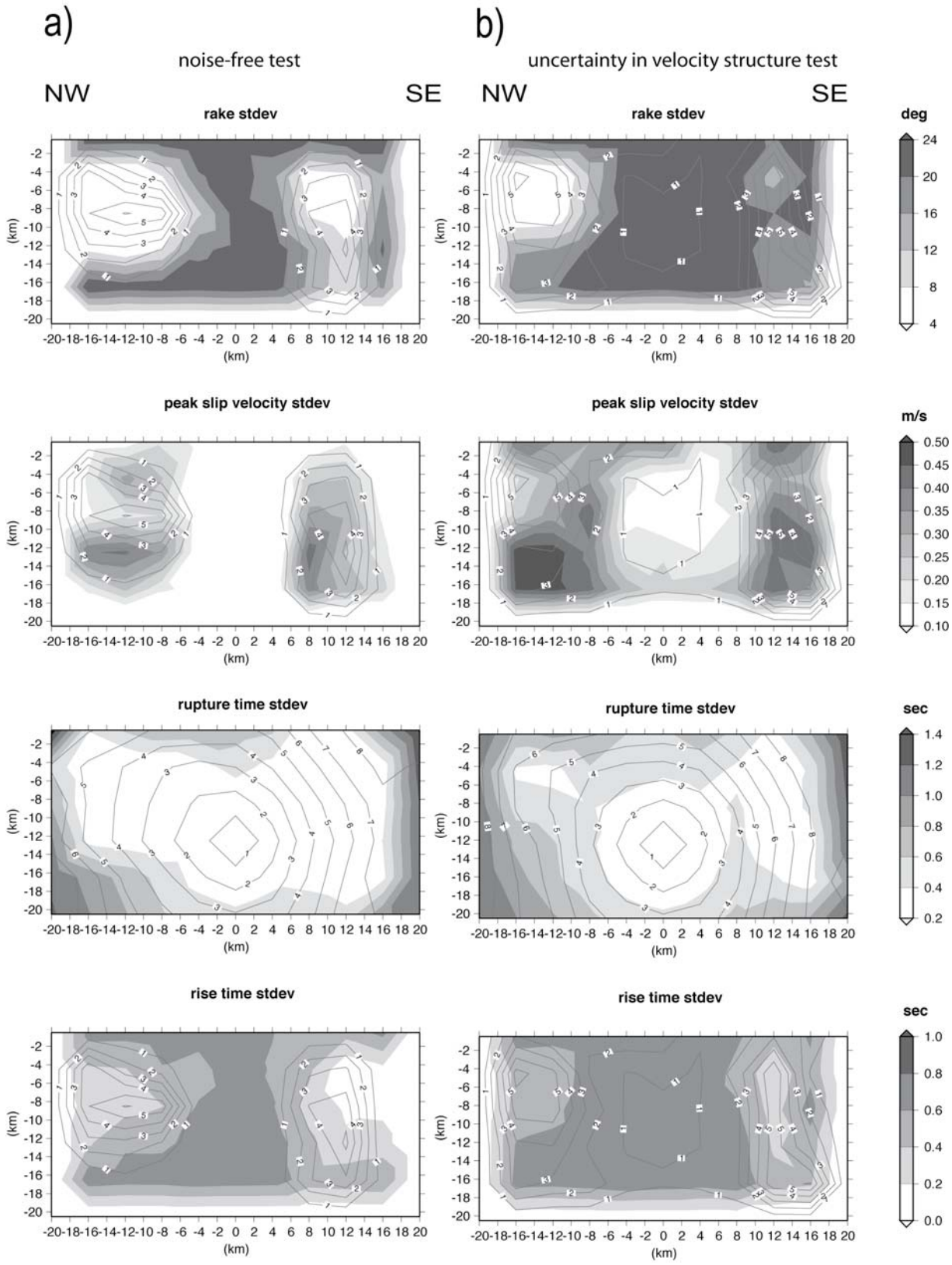
a)
noise-free test
NW
SE
b)
uncertainty in velocity structure test
NW
SE
rake stdev
deg
peak slip velocity stdev
m/s
rupture time stdev
sec
rise time stdev
sec
(km)

Figure 7

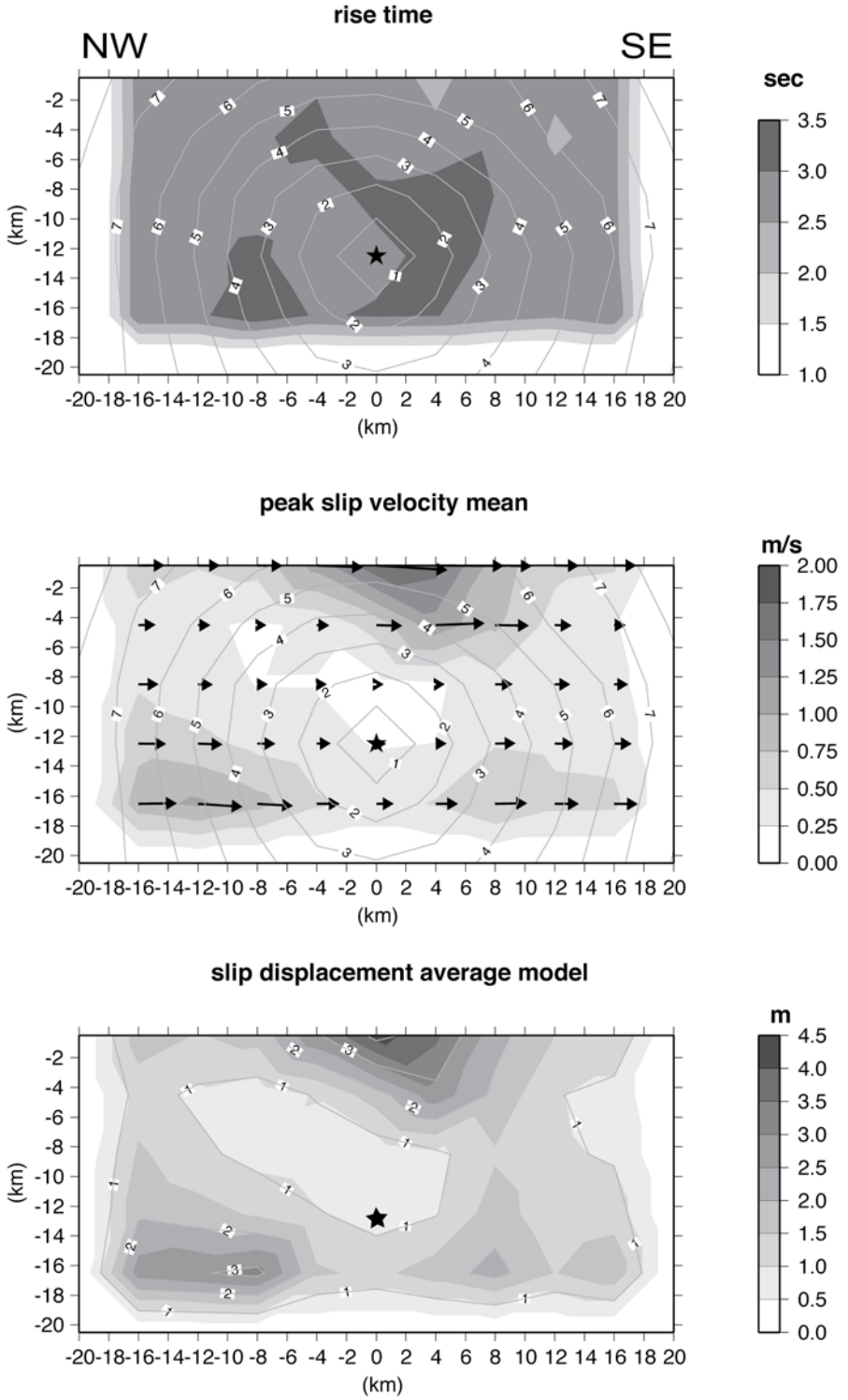
rise time
NW
SE
sec
3.5
3.0
2.5
2.0
1.5
1.0
(km)
(km)
peak slip velocity mean
m/s
2.00
1.75
1.50
1.25
1.00
0.75
0.50
0.25
0.00
(km)
(km)
slip displacement average model
m
4.5
4.0
3.5
3.0
2.5
2.0
1.5
1.0
0.5
0.0
(km)
(km)

Figure 8

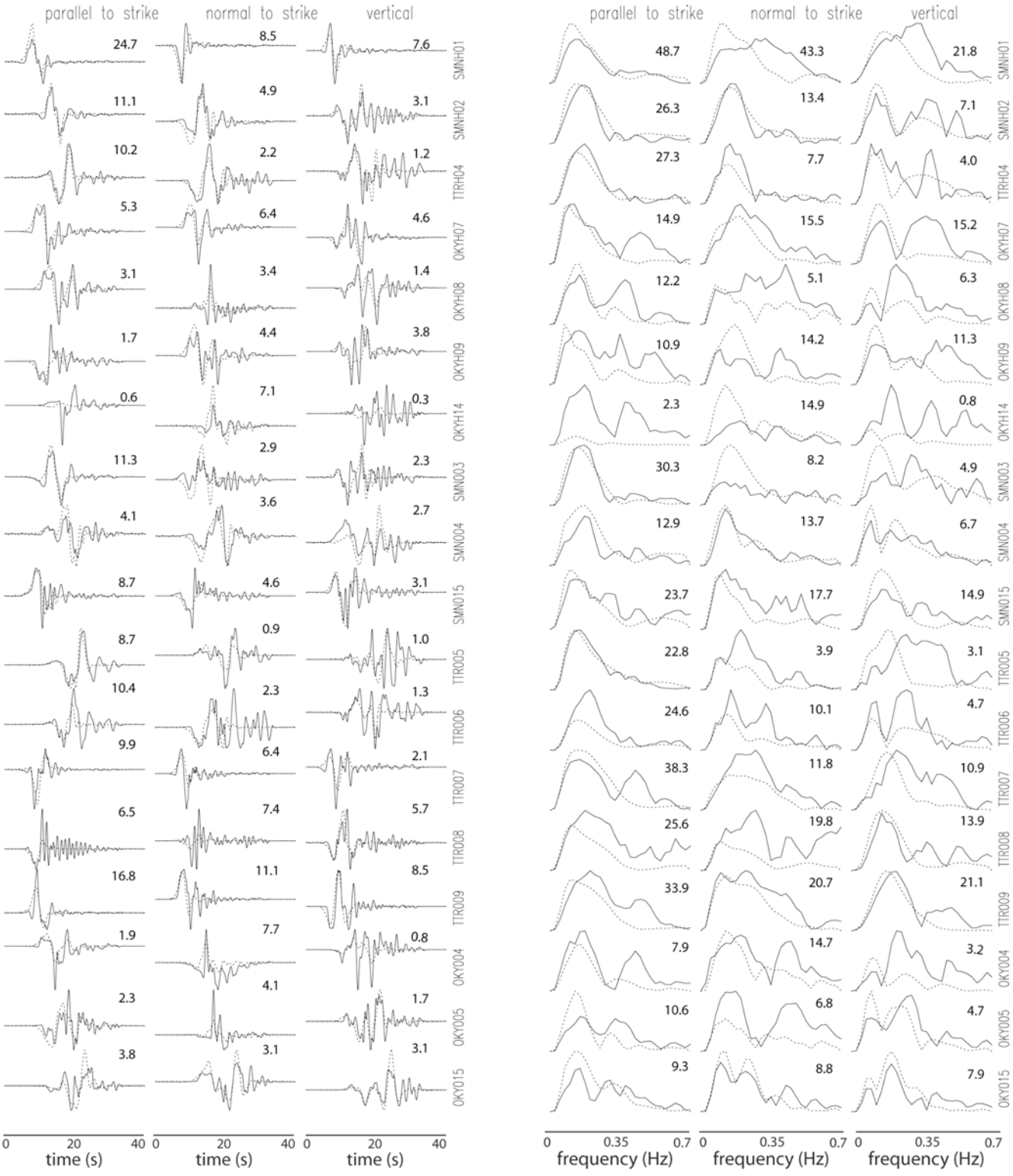
parallel to strike
normal to strike
vertical
24.7
11.1
10.2
5.3
3.1
1.7
0.6
11.3
4.1
8.7
8.7
10.4
9.9
6.5
16.8
1.9
2.3
3.8
8.5
4.9
2.2
6.4
3.4
4.4
7.1
2.9
3.6
4.6
0.9
2.3
6.4
7.4
11.1
7.7
4.1
3.1
7.6
3.1
1.2
4.6
1.4
3.8
0.3
2.3
2.7
3.1
1.0
1.3
2.1
5.7
8.5
0.8
1.7
3.1
SMNH01
SMNH02
TTRH04
OKYH07
OKYH08
OKYH09
OKYH14
SMN003
SMN004
SMN015
TTR005
TTR006
TTR007
TTR008
TTR009
OKY004
OKY005
OKY015
0
20
40
time (s)
48.7
26.3
27.3
14.9
12.2
10.9
2.3
30.3
12.9
23.7
22.8
24.6
38.3
25.6
33.9
7.9
10.6
9.3
43.3
13.4
7.7
15.5
5.1
14.2
14.9
8.2
13.7
17.7
3.9
10.1
11.8
19.8
20.7
14.7
6.8
8.8
21.8
7.1
4.0
15.2
6.3
11.3
0.8
4.9
6.7
14.9
3.1
4.7
10.9
13.9
21.1
3.2
4.7
7.9
0
0.35
0.7
frequency (Hz)

Figure 9

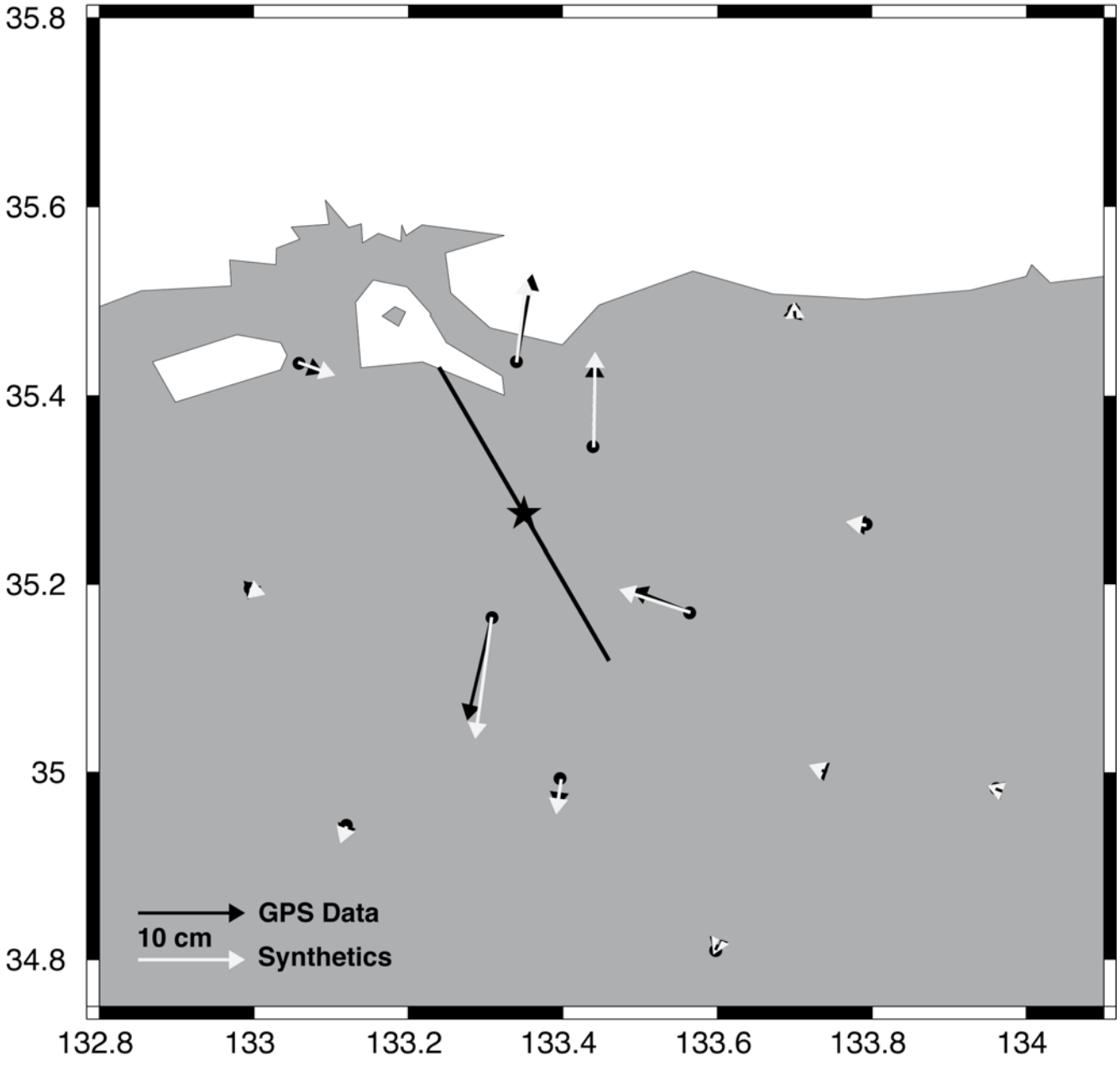
35.8
35.6
35.4
35.2
35
34.8
132.8
133
133.2
133.4
133.6
133.8
134
GPS Data
10 cm
Synthetics

Figure 10

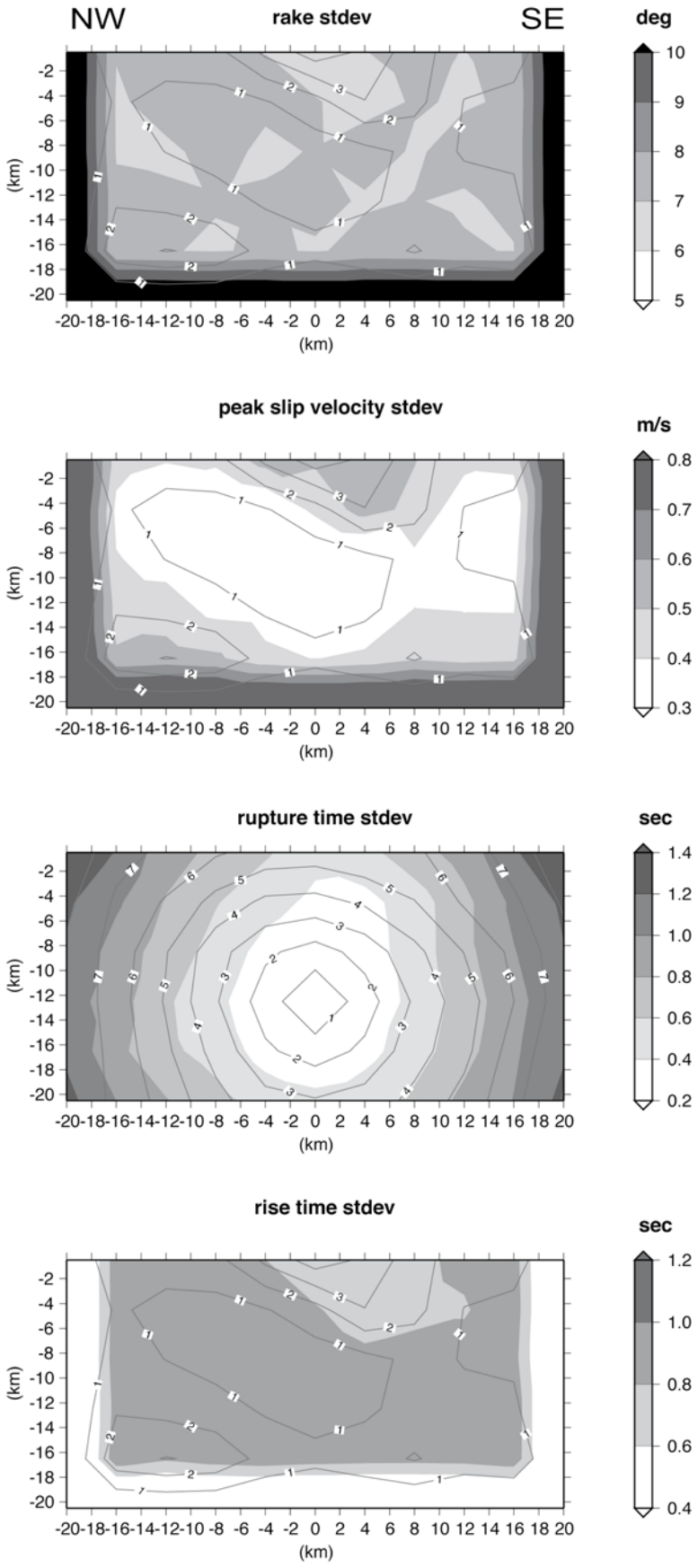
NW
rake stdev
SE
deg
10
9
8
7
6
5
peak slip velocity stdev
m/s
0.8
0.7
0.6
0.5
0.4
0.3
rupture time stdev
sec
1.4
1.2
1.0
0.8
0.6
0.4
0.2
rise time stdev
sec
1.2
1.0
0.8
0.6
0.4
(km)
-20 -18 -16 -14 -12 -10 -8 -6 -4 -2 0 2 4 6 8 10 12 14 16 18 20

Figure 11